



Oxygen Ablation during Atmospheric Entry: Its Influence on the Isotopic Composition of Micrometeorites

N. G. Rudraswami¹, M. Pandey¹, D. Fernandes¹, J. D. Carrillo-Sánchez^{2,3,4}, W. Feng^{2,5}, J. M. C. Plane², and V. P. Singh¹¹ National Institute of Oceanography (Council of Scientific and Industrial Research), Dona Paula, Goa 403004, India; rudra@nio.org, rudraswami@gmail.com² School of Chemistry, University of Leeds, Leeds LS2 9JT, UK³ Department of Physics, Catholic University of America, Washington, DC 20064, USA⁴ ITM Physics Laboratory, NASA/Goddard Space Flight Center, Code 675, Greenbelt, MD 20771, USA⁵ National Centre for Atmospheric Science, University of Leeds, Leeds LS2 9PH, UK

Received 2022 June 24; revised 2022 August 12; accepted 2022 August 27; published 2022 November 16

Abstract

Micrometeorites (MMs) offer glimpses of the diverse nature of parent bodies that accreted during the first few million years after the formation of the proto-Sun. The present work explores this by evaluating the ablation of oxygen from MMs during atmospheric entry, and the resulting effect on the oxygen isotopic composition. A Chemical Ablation MODEL (CABMOD) combined with the measured oxygen isotope composition of MMs, shows that at temperatures below 2000 K a relatively small percentage ($\sim 0\%$ – 5%) of oxygen ablates; the temperature is nevertheless sufficient to induce diffusion among the different silicate phases of MMs. The large $\delta^{18}\text{O}$ composition found within different MM types with low oxygen ablation indicates that exchange with atmospheric oxygen is insignificant during entry. Therefore, to explain the large $\delta^{18}\text{O}$ values existing in heated MMs, where oxygen ablation is less than a few percent, we propose that these particles are from distinct C-type asteroids that have undergone nebular gas exchange and/or aqueously altered in their parent bodies. This is supported by the evidence from unmelted MMs that have not exchanged oxygen during atmospheric entry or undergone ablation, but have large $\delta^{18}\text{O}$ values. However, the oxygen isotope composition of different types of cosmic spherules does not appear to vary systematically with temperature and could be due to the heterogeneity of their precursors. This investigation overall provides insights into the oxygen ablation of the particles during atmospheric entry, oxygen isotopic alteration, and the reservoirs of the diverse extraterrestrial objects that prevailed in the early solar system.

Unified Astronomy Thesaurus concepts: [Micrometeoroids \(1048\)](#); [Meteoroids \(1040\)](#)

1. Introduction

Micrometeorites (MMs) are extraterrestrial dust particles with sizes ranging from tens of microns to a few millimeters; they are collected ubiquitously on the Earth's surface, which shows the efficiency of dust release from a variety of parent bodies and, eventually, the safe passage of the particles through the Earth's atmosphere (e.g., Maurette et al. 1987; Taylor & Brownlee 1991; Taylor et al. 1998; Yada et al. 2004; Rochette et al. 2008; Onoue et al. 2011; Plane 2012; Prasad et al. 2013; Messenger et al. 2015; Noguchi et al. 2015; Rudraswami et al. 2016a; Genge et al. 2016). MMs normally represent diverse asteroidal and cometary parent bodies, based on their chemical and isotopic studies, which have been intensively investigated for decades (e.g., Brownlee et al. 1997; Taylor et al. 2000; Genge et al. 2008; Suavet et al. 2010; Cordier et al. 2011; Nesvorný et al. 2011; Gómez Martín et al. 2017; Suttle et al. 2019; Flynn et al. 2018). The oxygen isotopic compositions of MMs have revealed resemblances with diverse chondrites (carbonaceous, ordinary, enstatite) and their components (Ca, Al-rich inclusions (CAIs), chondrules, amoeboid olivine aggregates (AOAs), matrix and presolar silicates), although not in all cases (e.g., Engrand et al. 1999, 2005; Yada et al. 2005; Gounelle et al. 2009; Cordier & Folco 2014; Van Ginneken et al. 2017; Suttle et al. 2019; Goderis et al. 2020). Understanding the oxygen

isotope composition is not straightforward because meteoroid particles that hit the Earth's upper atmosphere experience partial or complete melting, ablation, and potential exchange with atmospheric species, consequently altering the chemical and isotopic composition of the precursor particle (e.g., Engrand et al. 1999, 2005; Yada et al. 2005; Cordier & Folco 2014; Rudraswami et al. 2020). Unlike meteorites, smaller dust particles decelerate at higher altitudes and are not large enough to produce ram pressure of bow shock as commonly found in larger meteorites (Love & Brownlee 1991). The interaction between gases in the Earth's atmosphere and a precursor particle during entry is a process that may significantly obscure the nature of the particle (Love & Brownlee 1993). For instance, determining the quantity of oxygen isotope contamination from the atmosphere, or changes due to ablation during entry, has always been challenging (Rudraswami et al. 2022). The oxygen isotope data acquired on different types of MMs has ranged widely, with $\Delta^{17}\text{O}$ from -6% to 3% , and some with relict grains have $\Delta^{17}\text{O}$ ranging from -23% to -15% (e.g., Engrand et al. 1999, 2005; Taylor et al. 2005; Yada et al. 2005; Matrajt et al. 2006; Cordier et al. 2011, 2012; Cordier & Folco 2014; Rudraswami et al. 2015, 2020, 2022; Van Ginneken et al. 2017; Suttle et al. 2019; Goderis et al. 2020). Oxygen isotope studies indicate that the majority of analyzed MMs are associated with carbonaceous chondrites, and a small percentage with ordinary chondrites; nevertheless, some MMs do not seem to be related to known chondritic precursors, e.g., cryptocrystalline spherule M03KS063 is ^{16}O -poor with a very high $\delta^{18}\text{O}$ value of $\sim 52\%$ and $\Delta^{17}\text{O} \sim 13\%$ (Yada et al. 2005); spherule AAS38-169-P59



Original content from this work may be used under the terms of the [Creative Commons Attribution 4.0 licence](#). Any further distribution of this work must maintain attribution to the author(s) and the title of the work, journal citation and DOI.

has a low $\delta^{18}\text{O}$ of $\sim 4\%$ and a high $\Delta^{17}\text{O}$ of $\sim 6\%$ (Rudraswami et al. 2016c); the oxygen isotope value of particle MM40 is similar to that of achondrites (Gounelle et al. 2009), indicating that the oxygen isotope composition of the precursor is heterogeneous with contributions from diverse sources. Barred texture particles have undergone heating and are expected to have high $\delta^{18}\text{O}$ as seen in various studies, although Yada et al. (2005) reported two such particles with ^{16}O -rich compositions. These two unusual barred ^{16}O -rich particles have $\delta^{18}\text{O}$ of -17% and -2% . However, unmelted MM TAM50-25 shows $\delta^{18}\text{O}$ similar to many heated cosmic spherules (Suttle et al. 2020), and similar values are seen in unmelted Antarctic MMs (Matrajt et al. 2006). In addition, it is challenging to determine the precursor of Calcium Aluminum Titanium (CAT) particles seen in most cosmic spherule collections produced from dust that has experienced extreme vaporization (Taylor et al. 2000; Yada et al. 2005; Rudraswami et al. 2020; Steven et al. 2020).

During the entry of MMs into the Earth's atmosphere they experience heating leading to alteration of their chemical and isotopic composition; the degree to which this occurs depends on their mass, chemical composition, entry velocity, and entry angle relative to zenith (Love & Brownlee 1993; Plane et al. 2015; Rudraswami et al. 2015, 2016a, 2016b, 2020; Genge 2017a, 2017b). Previous studies of MMs have shown large $\delta^{18}\text{O}$ values, which may indicate exchange with Earth's atmosphere (Engrand et al. 2005; Yada et al. 2005; Suavet et al. 2010; Cordier & Folco 2014; Rudraswami et al. 2015, 2016, 2020; Goderis et al. 2020). The purpose of this work is to quantify the oxygen elemental ablation for different types of carbonaceous (CI, CM, CV) chondrites along with ordinary (H, L, LL) chondrites using the Chemical ABlation MODel (CABMOD) (Vondrak et al. 2008). In addition, we explore whether it is possible to define the oxygen isotope pattern of cosmic spherules that have been altered by atmospheric exchange and/or elemental ablation during entry. This will better constrain the parent bodies, which is vital for understanding the diverse sources during the evolution of the early Solar system.

2. The Oxygen Isotope Composition of Micrometeorites

The oxygen isotope compositions of MMs for different textures overlap (Figure 1, references to the oxygen isotope data are provided in supplementary material), and they are often transitional and depend on several factors (such as the initial velocity, zenith angle of entry, size, mass, and initial chemical composition of the entering particle). Scoriaceous MMs are partially melted and highly vesicular particles that indicate the commencement of alteration of the particle; they are followed by various types of cosmic spherules such as porphyritic, barred, cryptocrystalline, glass, and CAT cosmic spherules (Genge et al. 2008). In the present study we take approximate values of temperature for this textural sequence as follows (Table 1): unmelted ($<1400\text{ K}$) $<$ scoriaceous ($\sim 1600\text{ K}$) $<$ porphyritic ($\sim 1700\text{ K}$) $<$ barred ($\sim 1900\text{ K}$) $<$ cryptocrystalline ($\sim 2000\text{ K}$) $<$ glass ($\sim 2300\text{ K}$) $<$ CAT ($\sim 2600\text{ K}$) (Hashimoto 1983; Love & Brownlee 1991; Genge et al. 1997, 2016, 2017; Toppani et al. 2001, Toppani & Libourel 2003; Van Ginnekan et al. 2017). The formation of I-type spherules is postulated to be caused by melting of dust with Fe-Ni grains at $\sim 2200\text{ K}$, as these particles can penetrate to greater depth owing to their higher density in the atmosphere at this temperature than S-type precursors (Genge et al. 2016).

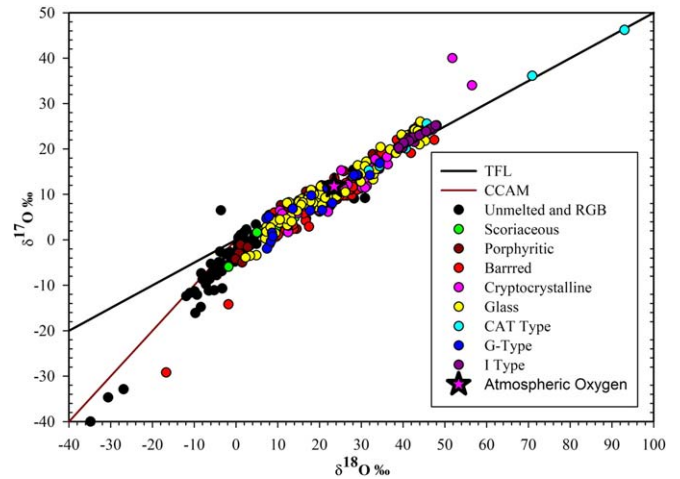


Figure 1. Compiled oxygen three-isotope plot for different types of MMs obtained from the literature (Clayton et al. 1986; Engrand et al. 1999, 2005; Taylor et al. 2005; Suavet et al. 2010; Cordier et al. 2011; Rudraswami et al. 2015, 2020; Van Ginnekan et al. 2017; Suttle et al. 2020; Goderis et al. 2020; Fischer et al. 2021). The TFL and CCAM lines are shown for reference. The atmospheric oxygen composition is from Thieme et al. (1995). The data on the oxygen isotope composition can be obtained from the references in the Appendix.

The oxygen isotope ratios of different chondrites, along with their components (chondrules, refractory inclusions, matrix), show a diverse composition, which is also reflected in different types of cosmic spherules; however, this diversity is complex in part because of atmospheric exchange and evaporation during entry (Love & Brownlee 1993; Rudraswami et al. 2015, 2016c, 2020). Some researchers have followed the approach of $\Delta^{17}\text{O} < 0\%$ (below the terrestrial fractionation line, TFL) to imply carbonaceous chondrites and $\Delta^{17}\text{O} > 0\%$ (above TFL) to indicate ordinary chondrites (Engrand et al. 1999; Cordier & Folco 2014; Rudraswami et al. 2015, 2020; Van Ginnekan et al. 2017; Suttle et al. 2019; Goderis et al. 2020). This approach has led to MMs mostly being characterized as carbonaceous chondrites ($>70\%$), with a smaller fraction of ordinary chondrites ($\sim 20\%$). However, this one-dimensional approach can sometimes lead to an inaccurate interpretation of some altered MMs, and needs to be rethought when considering that CR, Tagish Lake, and Comet Wild 2 samples exhibit FeO-rich type II chondrules that have formed much farther from the Sun and so tend to have $\Delta^{17}\text{O} \geq 0\%$ (e.g., Tenner et al. 2015; Defouilloy et al. 2017; Ushikubo & Kimura 2021). Further, the matrix of carbonaceous chondrites have $\Delta^{17}\text{O} \geq 0\%$, similar to that seen in many ordinary chondrites (Rowe et al. 1994; Clayton & Mayeda 1999; Yurimoto et al. 2008; Ireland et al. 2020). The small size of MMs (diameter in the range $\sim 10\text{--}2000\ \mu\text{m}$) that may have sampled from different types of chondritic precursors, along with chemical and isotopic alteration during atmospheric entry, makes it difficult to relate to their original source(s). Hence, a combination of chemical and isotopic studies along with an understanding of entry parameters should provide improved constraints for investigating the origins of individual MMs.

We have compiled oxygen isotope data (423) from the literature for (404) MMs that were analyzed using multiple techniques including Isotope Ratio Mass Spectrometry (IRMS) and in situ ion microprobe analyses (Clayton et al. 1986; Engrand et al. 1999, 2005; Taylor et al. 2005; Yada et al. 2005; Matrajt et al. 2006; Suavet et al. 2010; Cordier et al. 2011, 2012;

Table 1
Average and Range of $\delta^{18}\text{O}$ along with Peak Temperature of the Particles for Different Types of MMs

Type of MM	Number	Average $\delta^{18}\text{O}$ (‰)	Range of $\delta^{18}\text{O}$ (‰)	Peak Temperature (K)
Unmelted	65	-1.3	-39.7 to 30.9	<1400
Scoriaceous	14	11.5	-1.8 to 19.5	1600
Porphyritic	38	18.6	0.1 to 41.6	1800
Barred	89	22.9	-16.7 to 47.5	1900
Cryptocrystalline	43	25.9	10.5 to 56.5	2000
Glass	81	20.8	2.3 to 45.3	2300
CAT Type	6	52.7	31.8 to 93	2600
G Type	18	18.9	7.3 to 34.4	2000
I Type	50	42.4	38.8 to 48	2200

Note. The “Number” column indicates the number of MMs used to summarize the average and range of $\delta^{18}\text{O}$. The range of $\delta^{18}\text{O}$ indicates the spread in $\delta^{18}\text{O}$ values in the literature (Clayton et al. 1986; Engrand et al. 1999, 2005; Taylor et al. 2005; Suavet et al. 2010; Cordier et al. 2011; Rudraswami et al. 2015, 2020; Van Ginnekan et al. 2017; Suttle et al. 2020; Goderis et al. 2020; Fischer et al. 2021). The peak temperatures given in the table are approximate values that are taken from various references (rounded to the nearest hundred). The data for peak temperature are summarized using the following references: Hashimoto (1983), Love & Brownlee (1991), Genge et al. (1997), Toppani et al. (2001), Toppani & Libourel (2003), Genge et al. (2016, 2017), and Van Ginnekan et al. (2017).

Rudraswami et al. 2015, 2020; Van Ginnekan et al. 2017; Goderis et al. 2020; Fischer et al. 2021) to identify the effects of atmospheric entry and relate this to CABMOD data (Figure 1, references to the compiled oxygen isotope data are provided in supplementary material). The scoriaceous oxygen isotope composition has a relatively narrow spread in $\delta^{18}\text{O}$ among the cosmic spherules, along with relict-bearing particles. Additionally, data indicate that many unmelted particles are directly related to refractory inclusions and chondrule components (Genge et al. 2005; Taylor et al. 2010; Reshma et al. 2013; Rudraswami et al. 2022).

Unmelted and relict grain-bearing MMs are least altered since they have undergone heating to less than 1400 K (Toppani et al. 2001). In most cases, these particles have the potential to preserve oxygen isotopic composition and most of their $\delta^{18}\text{O}$ can be considered to represent their precursor signature (Engrand et al. 1999; Gounelle et al. 2005; Rudraswami et al. 2016a; Suttle et al. 2020). The study by Matrajt et al. (2006) on 22 unmelted MMs categorized them into fine grained, coarse grained as well as composite types, which show an unexpectedly high variability in $\delta^{18}\text{O}$ ranging from $\sim 3\%$ to 60% ; six scoriaceous particles exhibited a similar range ($\sim 29\%$ – 52%). These data ranges for oxygen isotopes are comparable to those found in many of the most melted particles, and exhibit a large disparity with the data for relict-bearing and unmelted particles from other groups (Greshake et al. 1996; Engrand et al. 1999; Gounelle et al. 2005; Yada et al. 2005; Rudraswami et al. 2016a; Suttle et al. 2020). Matrajt et al. (2006) suggested that the large spread is caused by diverse or heterogeneous parent bodies contributing to the samples of MMs. The results on scoriaceous particles from Matrajt et al. (2006) and Rudraswami et al. (2020) disagree, with the former finding that all particles had average $\delta^{18}\text{O}$ greater than 29% , while the latter found an average $\delta^{18}\text{O}$ less than 20% . The unmelted particles are expected to fall close to the CCAM (carbonaceous chondrite anhydrous mineral) line on an oxygen three-isotope plot with lower $\delta^{18}\text{O}$ values (Figure 1). Nevertheless, the identification of the parent body of unmelted grains is challenging due to the cumulative influence of atmospheric entry and terrestrial weathering effects, leading to inconsistent findings (Suttle et al. 2019). Small MMs show an oxygen isotope composition similar to that of carbonaceous

chondrites, signifying a similar isotopic reservoir (Gounelle et al. 2005).

The porphyritic and barred cosmic spherules form at nearly the same peak temperatures, ~ 1800 and 1900 K, respectively. In 38 porphyritic spherules the average $\delta^{18}\text{O}$ is $\sim 19\%$, ranging from $\sim 0\%$ to 42% . In the case of 89 barred cosmic spherules, the average $\delta^{18}\text{O}$ is $\sim 23\%$, ranging from $\sim 8\%$ to 48% . Cryptocrystalline cosmic spherules, which are formed at slightly lower temperatures than glass spherules, exhibit an average $\delta^{18}\text{O}$ of $\sim 26\%$, ranging from 11% to 57% . Glass spherules show an average $\delta^{18}\text{O}$ of $\sim 21\%$, ranging from $\sim 2\%$ to 45% . CAT spherules, which are the cosmic spherules heated to the highest temperatures, are categorized by a high degree of evaporative mass loss with $\text{Mg}/\text{Si} > 1.7$ and an enrichment in refractory Ca, Ti, and Al. Here the average $\delta^{18}\text{O}$ is around 53% , ranging from $\sim 32\%$ to 93% (Yada et al. 2005; Rudraswami et al. 2020). I-type cosmic spherules have a relatively narrow $\delta^{18}\text{O}$ range of 39% – 48% , with an average of 42% (Figure 1).

3. The Chemical Ablation Model (CABMOD)

The evolution of the MM precursor in the Earth’s atmosphere is constructed by using CABMOD. The model describes frictional heating, melting, phase transitions, and vaporization of a particle with specified mass, entry velocity, and entry angle (Vondrak et al. 2008; Plane 2012; Carrillo-Sánchez et al. 2015). A detailed flowchart and the differential equations and parameters in the model are given in Vondrak et al. (2008). The CABMOD model consider the loss of oxygen due to vaporization and does not include the diffusion of atmospheric oxygen to the particle. The model incorporates the effect of chemical composition of the particles during entry for different types of preferred chondritic composition (CI, CM, CV, H, L, LL). Particle density is a variable parameter, since the densities of interplanetary dust particles (IDPs) captured in the stratosphere, although peaked at $\sim 2 \text{ g cm}^{-3}$ similar to CI chondrites, exhibit a spread up to 3.5 g cm^{-3} , i.e., similar to the densities of ordinary chondrites (Flynn & Sutton 1990; Love et al. 1994; Flynn et al. 2018; Rojas et al. 2021). Previous studies on MMs have assumed that their precursors are essentially either CI or CM chondrites, though other chondrites need to be treated for completion (e.g., Brownlee et al. 1997; Taylor et al. 2000; Prasad et al. 2013, 2015; Rudraswami et al. 2019).

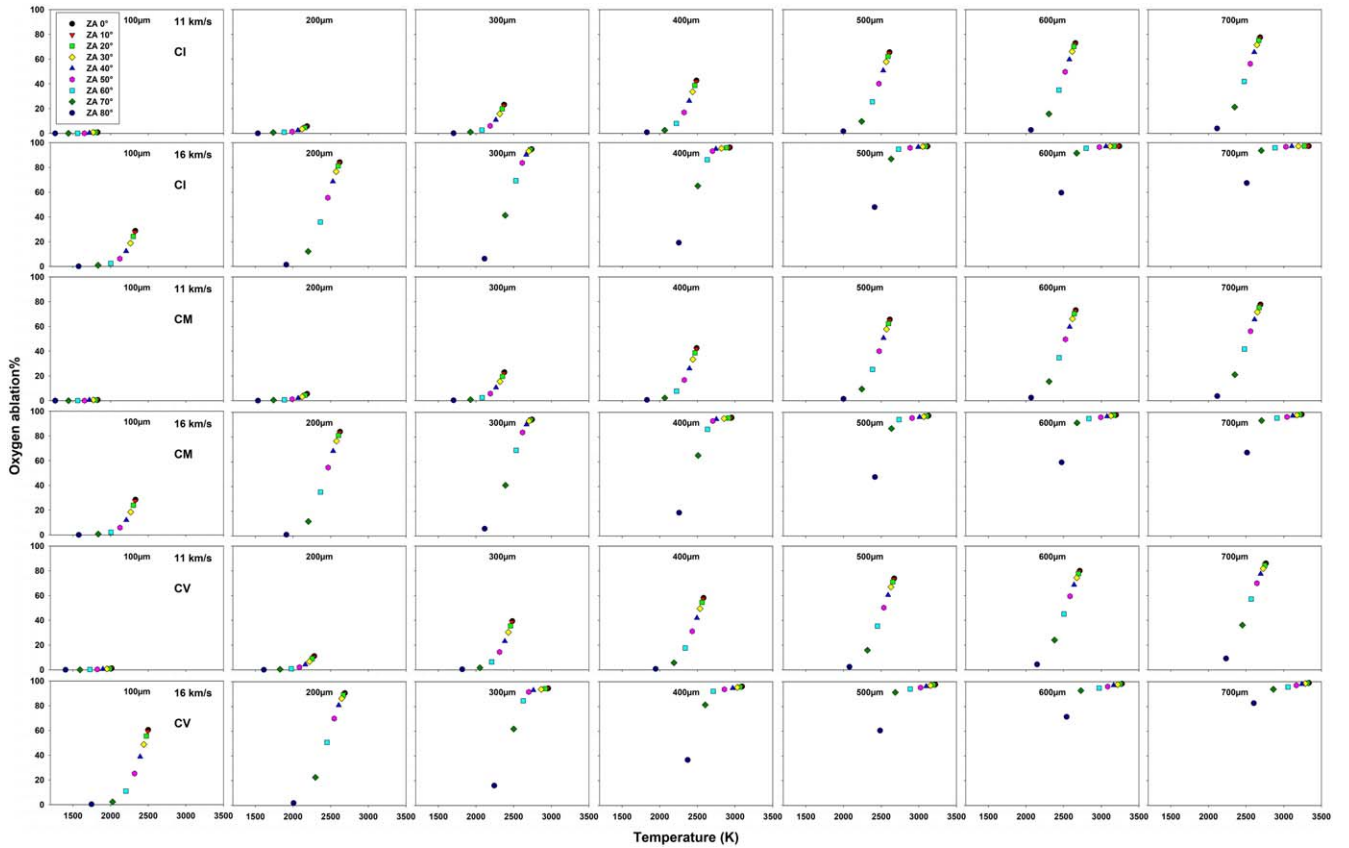


Figure 2. Oxygen ablation percentage vs. temperature derived from the CABMOD for different types of carbonaceous (CI, CM, CV) chondritic precursors with sizes ranging from 100 to 700 μm and zenith angle ranging from 0° to 80° entering at velocities of 11 km s^{-1} and 16 km s^{-1} .

Earlier ablation models only considered the variation in physical parameters of the particles such as radius, temperature, density, and mass, along with entry velocity and angle (Flynn 1989a, 1989b; Love & Brownlee 1991). Likewise, some studies on the elemental ablation of various chondrites took into account ablation of the major (Mg, Si, Fe) and minor (Na, Ca, Al) elements along with these physical properties (Rudraswami et al. 2015, 2018). These studies were constrained to 16 km s^{-1} , because at higher entry velocities particles tend to ablate completely (Vondrak et al. 2008; Carrillo-Sánchez et al. 2015; Rudraswami et al. 2016b). In contrast to earlier work, the present study includes oxygen elemental ablation for different entry parameters and types of precursors. The variation in the alteration of the oxygen composition of different chondrites is controlled by zenith entry angle, entry velocity, size, and density. We therefore use the CABMOD model to determine the percentage of elemental oxygen ablation in a particle over a range of sizes (diameter of 100–700 μm), entry velocities (11–72 km s^{-1} in steps of 5 km s^{-1}), and zenith angles (0° – 90° in steps of 5°). The results are shown in Figures 2–5. The published analyses of the oxygen isotope composition of the different MM types (unmelted, scoriaceous, porphyritic, barred, cryptocrystalline, glass, and CAT) are used for correlation with the elemental oxygen ablation and temperature in Figure 6.

It should be noted that CABMOD does not include the loss of oxygen from organic matter that decomposes at considerably lower temperature than the melting temperature of silicates. The experimental system of Bones et al. (2022) measured the pyrolysis kinetics of carbonaceous chondrite samples, in the size range of MMs, by mass spectrometric detection of CO_2

and SO_2 at temperatures ranging between 625 and 1300 K. In fact, most of the ablated organic matter is mainly released as CO_2 , and perhaps the direct release as atomic oxygen is marginal. Genge (2017b) shows that vesicle formation of the particles during entry changes the density, causing a parachute effect due to rapid deceleration, which is less marked in those particles that are melted. The vesicular parachuting is not incorporated in the CABMOD model, but we can infer that a decrease in the rate of heating would decrease the amount of O vaporization.

4. Elemental Oxygen Ablation of MMs during Atmospheric Entry

MMs that reach the Earth’s surface have survived heating and ablation during atmospheric entry (Maurette et al. 1991; Love & Brownlee 1993; Taylor et al. 1998; Yada et al. 2004; Genge et al. 2008; Prasad et al. 2013; Rudraswami et al. 2020). In CABMOD, particle mass loss occurs through sputtering by inelastic collisions (relatively minor), and through evaporation of atoms during the ablation process that occurs at an altitude of ~ 80 – 140 km (Vondrak et al. 2008). The amount of ablation a particle experiences is proportional to the peak temperature reached during entry and the length of time the particle spends above its melting point. The elemental ablation profile is typically bimodal: the most volatile elements, Na and K, are lost initially, much before the particle reaches 1800 K, and this is followed by major element loss of Fe, Si, and Mg at $\sim 2000 \text{ K}$ (Rudraswami et al. 2016b). The minor elements Ca, Al, and Ti are refractory in nature and do not get depleted until the temperature exceeds 2000 K (Vondrak et al. 2008).

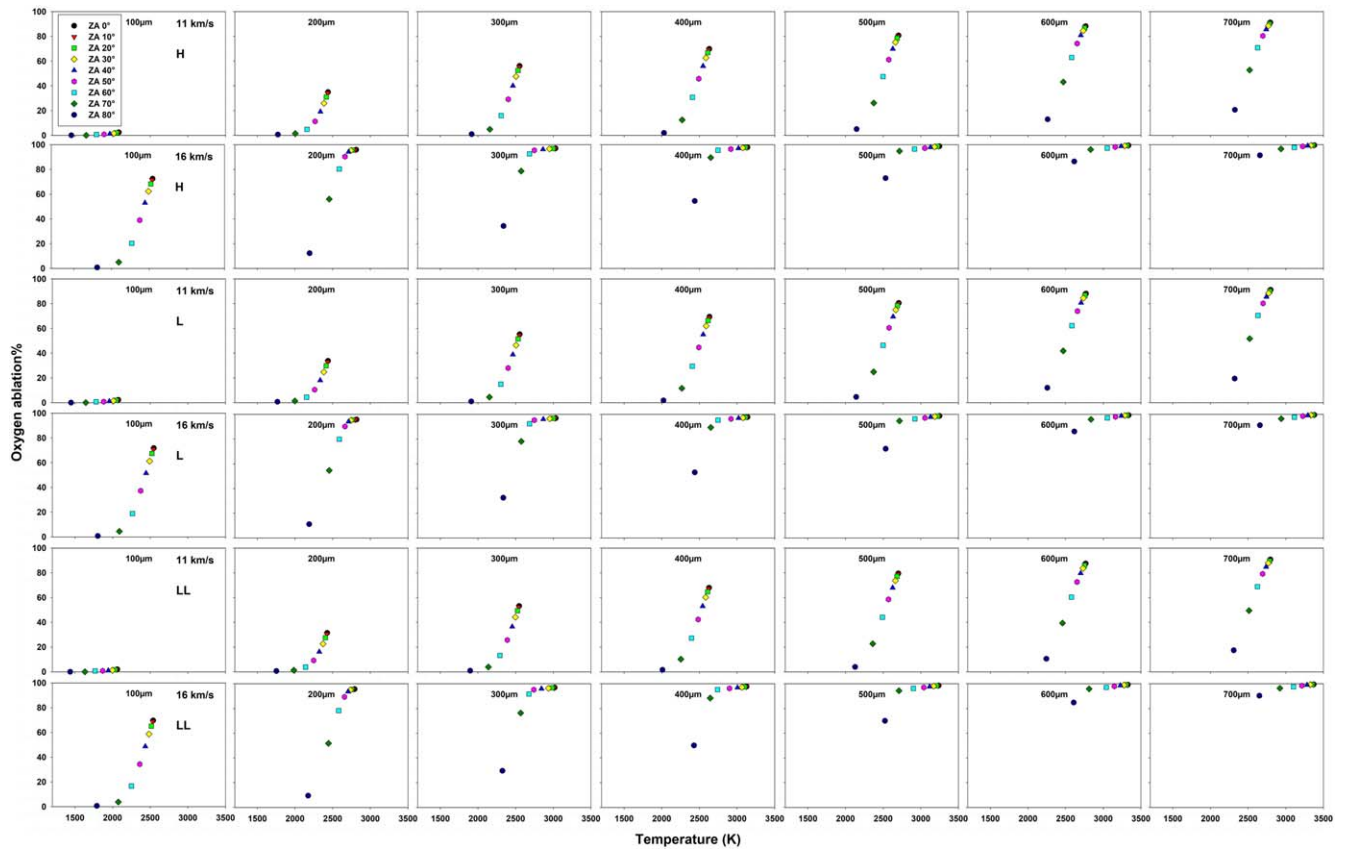


Figure 3. Oxygen ablation percentage vs. temperature derived from the CABMOD for different types of ordinary (H, L, LL) chondritic precursors with sizes ranging from 100 to 700 μm and zenith angle ranging from 0° to 80° entering at velocities of 11 km s^{-1} and 16 km s^{-1} .

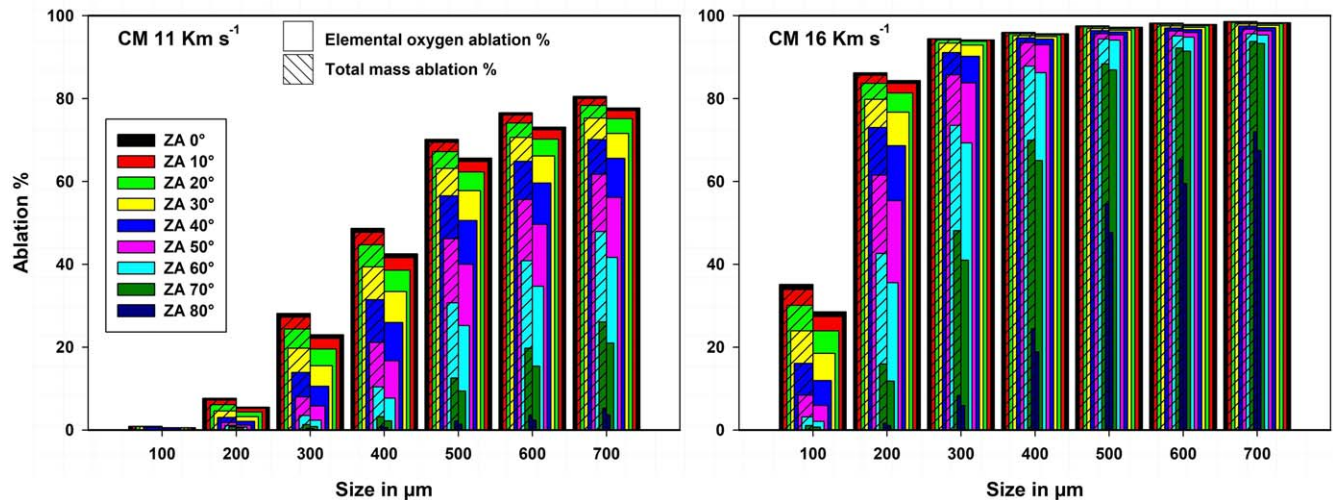


Figure 4. Elemental oxygen ablation and total mass ablation percentage for CM chondrites for various sizes ranging from 100 to 700 μm and zenith angle ranging from 0° to 80° entering at velocities of 11 km s^{-1} (left) and 16 km s^{-1} (right).

The Meteor Ablation Simulator (MASI), an experimental setup established at the University of Leeds, has been used to refine and validate the CABMOD model with experimental measurements of the metals evaporated from meteoric samples by Laser-Induced Fluorescence (LIF; Bones et al. 2016; Gómez Martín et al. 2017). Based on the MASI experimental results, the CABMOD model reproduces satisfactorily the measured peak ablation pulses and the relative ablated fractions of Na (Gómez Martín et al. 2017) and other meteoric

metals such as Fe, P, Ni, or Mg (Bones et al. 2018, 2019; Carrillo-Sánchez et al. 2020). Understanding the oxygen elemental ablation in particles is crucial for determining the fractionation process that may have taken place during entry because oxygen is the most abundant elemental constituent of metal oxides and silicate minerals. However, it remains uncertain exactly how much oxygen in MMs has been impacted by physical-chemical processes during entry and mixing with atmospheric oxygen. In addition, different phases

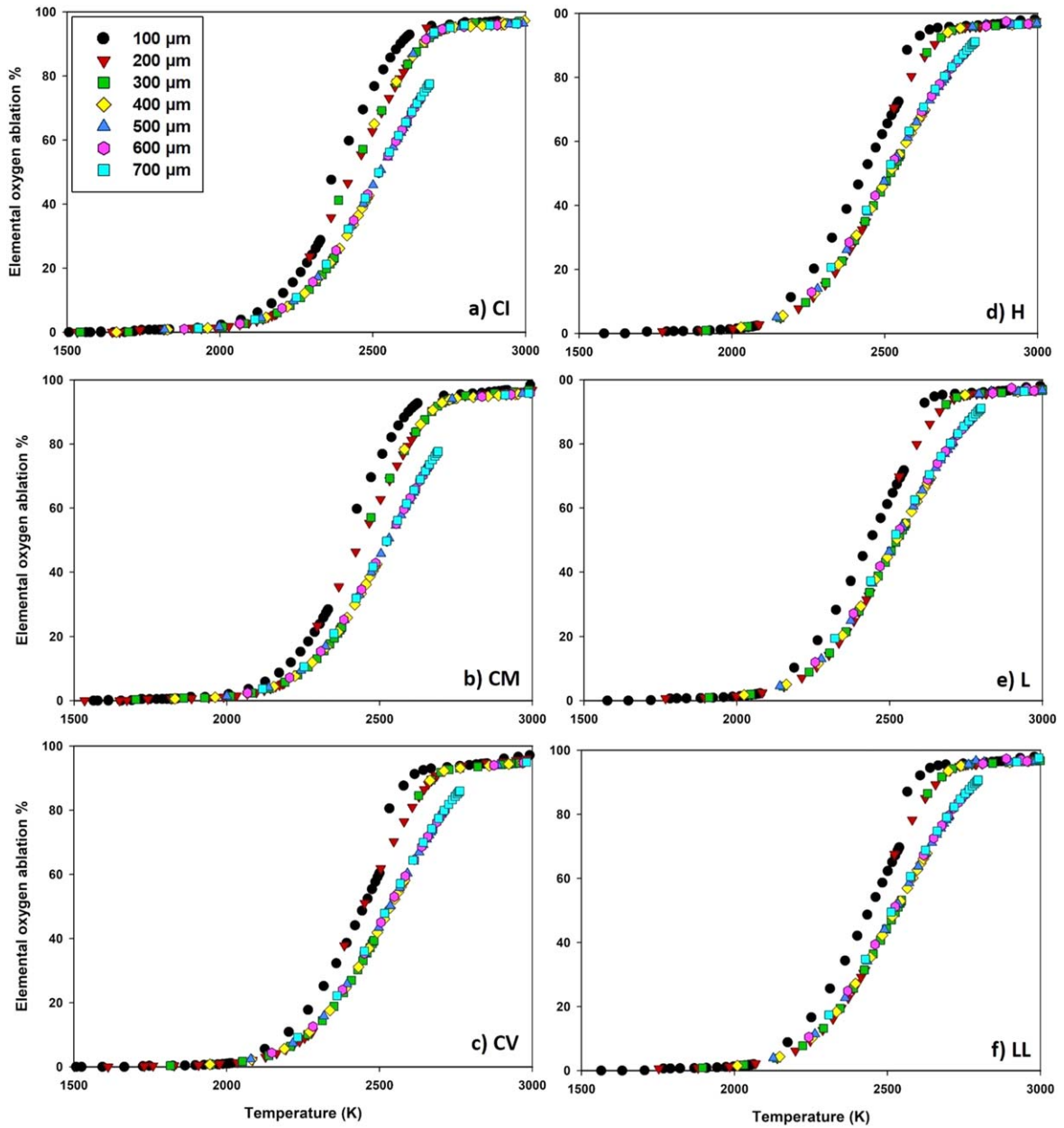


Figure 5. Elemental oxygen ablation percentage derived from CABMOD for carbonaceous (CI, CM, CV) and ordinary (H, L, LL) chondritic precursor sizes ranging from 100 to 700 μm . The graphs consider only oxygen ablation percentage as a function of temperature.

may get mixed due to diffusion if they are unmelted or partially altered. Thermal gradients within the particle may lead to subtle changes in some portions, with the remainder retaining the original signatures in minimally heated particles (Suttle et al. 2020). The magnetite rims that are found on unmelted MMs imply atmospheric oxygen exchange well below the melting temperature of the particle. Nevertheless, the possibility of oxygen isotope exchange deep within the unmelted particles may be minimal as solid diffusion is very slow and can be considered as preserved.

Although significant ablation of oxygen is not predicted by CABMOD to occur for particles that have experienced temperatures < 2000 K (Figure 5), the diffusion of oxygen within the particle’s different phases cannot be ruled out. The oxygen ablation percentages, based on the temperatures of various chondritic precursors, are provided in Figures 2 and 3 for

different entry velocities and zenith angles (ZAs). The oxygen ablation for different chondritic precursors shows an initial sigmoidal rise in ablation with temperature irrespective of their chemical composition and density (Figures 2, 3, and 5). Above 2500 K, more than 60% of the elemental oxygen ablates (Figure 5).

The model predicts that ordinary chondrite precursors have a higher percentage of oxygen ablation than carbonaceous chondrites (Figures 2 and 3). CI and CM chondrites have similar oxygen ablation percentages with respect to their peak temperatures among the carbonaceous precursors, while CV chondrite shows a slightly higher percentage: e.g., at an entry velocity of 11 km s^{-1} , $ZA = 0^\circ$, and a particle size of $200 \mu\text{m}$, the total oxygen ablation percentage is $\sim 6\%$ for CI and CM chondrites, while it is $\sim 11\%$ for CV chondrites. However, for similar atmospheric entry parameters, the model for ordinary

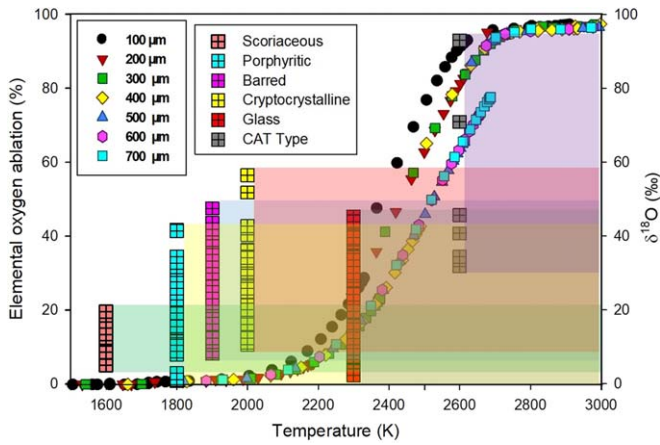


Figure 6. The oxygen isotope composition ($\delta^{18}\text{O}$) from the literature (read data on the right-hand side for oxygen isotope values vs. temperature) for different textures of cosmic spherules along with temperature. The shaded regions for different textures illustrate the spread in $\delta^{18}\text{O}$ for the particles that have experienced different entry temperature. The left-hand side shows the elemental oxygen ablation percentage vs. temperature for CM chondrite (of Figure 4) for sizes ranging from 100 to 700 μm . The graph also suggests that elemental ablation is insignificant below a temperature 2000 K.

chondrites suggests that this percentage is substantially greater, $\sim 35\%$ for H, $\sim 34\%$ for L, and $\sim 31\%$ for LL. The peak temperature for a particle at 5% oxygen ablation is ~ 2400 K, at 10% it is ~ 2500 K, and at 30% it is ~ 2700 K. For entry velocity of 16 km s^{-1} , $\text{ZA} = 0^\circ$, and particle size $200 \mu\text{m}$ the total oxygen ablation percentage for CI and CM is $\sim 84\%$ (Figure 4), while it is more than 90% for CV, and exceeds 95% for ordinary H, L, and LL chondrites. At 11 km s^{-1} , a particle smaller than $100 \mu\text{m}$ exhibits a low oxygen ablation percentage regardless of ZA, i.e., the particle retains most of its primitive elemental oxygen because small and slow entry particles ablate less efficiently (Figures 2–4). However, at an entry velocity of 16 km s^{-1} , $\text{ZA} = 0^\circ$, and particle size of $100 \mu\text{m}$ this percentage is $\sim 29\%$ for CI and CM, while it is $\sim 61\%$ for CV and $\sim 73\%$, 72% , and 70% for ordinary H, L, and LL chondrites, respectively. Furthermore, particles larger than $400 \mu\text{m}$ at 11 km s^{-1} and $\text{ZA} = 0^\circ$ exhibit $\sim 43\%$ oxygen ablation for CI and CM precursors, $\sim 48\%$ for CV chondrites, and $\sim 70\%$ for ordinary chondrites. If these particles enter at the minimum velocity of $\sim 11 \text{ km s}^{-1}$, at $\text{ZA} > 60^\circ$, the ablative mass loss of oxygen is $< 50\%$, which permits the original oxygen to be preserved with the least alteration; however, at 16 km s^{-1} , this percentage is $> 90\%$ apart from those having the largest ZAs ($> 80^\circ$) (Figure 4). The total mass ablation from molten silicate particles can be related to the oxygen elemental ablation. This is shown in Figure 4 for the case of CM chondrites with velocities of 11 and 16 km s^{-1} . The notable trend observed here is that, as the size of the particle increases, the oxygen and total mass ablation also increase.

This process of evaporation contributes to oxygen isotopic fractionation in the samples. CABMOD indicates that carbonaceous CI and CM precursors entering at 11 km s^{-1} with a size $< 200 \mu\text{m}$ should preserve precursor oxygen, irrespective of entry zenith angle (Figures 2–4). A CV precursor is found to be similar to ordinary chondrites such as H, L, and LL, for which this window shrinks to a particle size of $< 100 \mu\text{m}$. Particles arriving at 16 km s^{-1} , on the other hand, have a reasonably large oxygen ablation percentage of $> 60\%$ at a size of $> 400 \mu\text{m}$ for ZAs 0° – 70° . Nonetheless, some particles

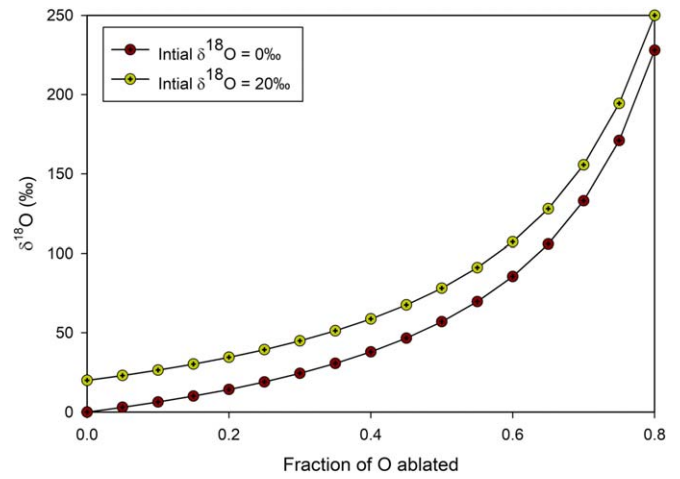


Figure 7. The oxygen isotope composition ($\delta^{18}\text{O}$) vs. fraction of oxygen ablated. The initial compositions of $\delta^{18}\text{O}$ considered are 0‰ and 20‰ .

entering at 16 km s^{-1} with a particle size of $\leq 100 \mu\text{m}$ and $\text{ZA} = 0^\circ$, particularly CI and CM chondrites, show a lower oxygen ablation percentage of $< 30\%$, and thereby have minimal alteration from their original oxygen composition (Figure 4). However, for CV and ordinary chondrites, this percentage approaches $> 60\%$. CABMOD indicates ordinary chondritic particles are more likely to ablate a large portion of their oxygen, whereas carbonaceous precursors, except for CV, have a better chance of retaining their original oxygen content and can reach the Earth with the least amount of oxygen change.

5. Relation between O Ablation and Oxygen Isotope Composition of MMs

Elemental (Mg, Si, Fe) changes have been evaluated and constrained by Rudraswami et al. (2015); however, elemental oxygen ablation and the associated variation in oxygen isotopic ratios within different types of cosmic spherules, arriving with different entry parameters, are not yet upheld in detail due to the complex nature of atmospheric exchange and evaporation of the particles that enter. Until the particle temperature reaches ~ 2000 K, oxygen ablation during entry is insignificant, but it rises rapidly above this temperature (Figures 5 and 6). This remains valid irrespective of the entry angle and size and type of precursor. $\delta^{18}\text{O}$ should increase once ablation commences because, according to Langmuir evaporation described by the Herz–Knudsen relation which is used in CABMOD (Vondrak et al. 2008), the rate of evaporation of the two O isotopes will scale as the inverse of the square root of their mass, i.e., ^{18}O will evaporate 0.943 times as quickly as ^{16}O . The resulting increase in $\delta^{18}\text{O}$ with the fraction of oxygen ablated from a particle is illustrated in Figure 7 for two cases where the initial oxygen $\delta^{18}\text{O}$ composition of the precursor has a value of $\sim 0\text{‰}$ or 20‰ . The initial $\delta^{18}\text{O}$ composition (0‰ and 20‰) increases to $\sim 50\text{‰}$ after $\sim 45\%$ and $\sim 35\%$ of the oxygen ablates, respectively; and for $\delta^{18}\text{O}$ to reach $\sim 100\text{‰}$, oxygen ablation of $\sim 65\%$ and $\sim 60\%$ is required, i.e., the difference in required oxygen ablation for the two cases becomes narrower at higher oxygen ablation percentages. There may not be any significant atmospheric exchange until a particle melts (diffusion in the solid is too slow), but once the particles melt and reach a temperature of 2000 K, the rate of O evaporation will

significantly exceed uptake of atmospheric O. So it can be expected that atmospheric exchange would only be important between the melting temperature and the temperature at which there is significant ablation of Fe, Mg, Si, and O. The atmospheric oxygen added by the formation of magnetite rims on the surfaces of the unmelted or partially melted particles has not been taken into account because diffusion of oxygen in a solid is a very slow process. The formation of a magnetite rim on the surface of particles during entry, usually seen in many partially melted or unmelted relict-bearing particles, does not seem to penetrate to the depth of the particles (Rudraswami et al. 2016a, 2016c).

The CI, CM, and CV chondritic precursor exhibit a similar trend where oxygen ablation starts: as the size of the particle increases and the zenith angle decreases the oxygen ablation percentage increases (Figure 2). This is also true for ordinary chondritic precursors (Figure 3), except that the oxygen ablation percentage is greater than that of the carbonaceous precursor for a given ZA and size (Table 2). However, the micrometeoroid's oxygen ablation percentage is relatively low at an entry velocity of $\sim 11 \text{ km s}^{-1}$ and rises rapidly for an entry velocity $\geq 16 \text{ km s}^{-1}$ (Figure 4). Studies of elemental composition on large samples of cosmic spherules have shown these to be very similar to CM-type chondrites (Brownlee et al. 1997). For instance, a CM chondritic precursor was used to evaluate the correlation between total mass ablation and oxygen elemental ablation for ~ 11 and 16 km s^{-1} (Figure 4). There is almost one-to-one correlation for the two ablations, where for 11 km s^{-1} the ablation is less than 10% for size (diameter) of $\sim 200 \mu\text{m}$, ZA 0° – 80° , and rises rapidly for sizes $> 300 \mu\text{m}$. However, for 16 km s^{-1} the oxygen elemental and mass ablation are $> 80\%$ for $200 \mu\text{m}$ and ZA 0° , but decrease with increasing ZA (Figure 4). Comparable and much larger ablation trends can be anticipated for different types of carbonaceous and ordinary chondritic precursors (Figure 4 is plotted only for CM chondrite type precursors). This result indicates that total mass ablation dominated by the major elements (Fe, Mg, Si) has elemental oxygen being ablated in equivalent amounts from the precursor during entry. However, identifying the precursor from these largely ablated particles (such as glass and CAT) becomes more challenging for the reasons above.

The degree of change in oxygen isotopes of S-type cosmic spherules during their atmospheric entry is largely governed by the temperature of the particles attained during entry (Engrand et al. 1999; Yada et al. 2005; Matrajt et al. 2006; Rudraswami et al. 2015, 2020, 2022; Van Ginneken et al. 2017; Suttle et al. 2019). The scoriaceous particles appear to show a narrow spread of $\delta^{18}\text{O}$, while it seems to be very similar for porphyritic, barred, and cryptocrystalline spherules where the peak temperature attained by these particles is less than 2000 K. Glass spherules experience peak temperatures around 2300 K and the resulting significant ablation of oxygen causes a similar spread of $\delta^{18}\text{O}$. However, CAT spherules are different and seen to have a wider spread for $\delta^{18}\text{O}$ that goes up to $\sim 93\%$ (Yada et al. 2005; Rudraswami et al. 2020), which is explained (see Figure 7) by the much higher temperatures experienced compared with other spherules (Figures 1 and 6). Because most micrometeoroids undergo thermal processing that modifies their initial O-isotopic compositions, the O-isotopic composition of these particles before entry remains unknown. Even the unmelted particles have undergone some alteration or diffusion

between the phases, but oxygen isotope data from these particles can be interpreted as preserved. Unmelted particles retain the isotopic composition of their precursors, in contrast to I-type cosmic spherules, which derive oxygen solely during their atmospheric entry (Tomkins et al. 2016; Pack et al. 2017; Fischer et al. 2021).

The measured $\delta^{18}\text{O}$ values at an altitude of $\sim 60 \text{ km}$ are around 24% (Thiemens et al. 1995; Pack et al. 2017). However, there are many particles that are close to or even exceed this value, making it more challenging to assess the size of contribution from exchange during entry, even when the oxygen ablation of the particle is negligible. Fine-grained MM SP007-P257, which should not have undergone heating beyond 1400 K, revealed higher $\delta^{18}\text{O}$ values (Rudraswami et al. 2022), which was interpreted as the particle inheriting the high $\delta^{18}\text{O}$ values of its precursor. This is also similar to numerous cases related to unmelted MMs (Matrajt et al. 2006; Suttle et al. 2020).

Some hydrated carbonaceous chondrites have shown intense aqueous alteration, resulting in higher $\delta^{18}\text{O}$ values (Ikeda & Prinz 1993; Goodrich et al. 2019; Kebukawa et al. 2019; King et al. 2019; Suttle et al. 2020). The CY chondrites, which are ^{16}O -poor with an average $\delta^{18}\text{O}$ of $\sim 22\%$, are considered to be the isotopically heavier carbonaceous chondrites (Clayton & Mayeda 1999; Tonui et al. 2014; Suttle et al. 2020). The clast in the Zag meteorite also has a similar $\delta^{18}\text{O}$ value (Kebukawa et al. 2019). These CY chondrites are on the TFL (Figure 5 of Suttle et al. 2020), similar to many cosmic spherules. Note that the spread in the $\delta^{18}\text{O}$ values of MMs much beyond CY values can be related to oxygen ablation during entry (Figures 6 and 7). The contribution of ^{16}O -poor isotopic samples from scoriaceous, porphyritic, barred, and cryptocrystalline particles may be from those meteorites that are still not a part of our collection and may represent diverse small solar system bodies. However, in the case of glass and CAT spherules it is significant oxygen ablation during entry that controls the high $\delta^{18}\text{O}$ values (Figures 6 and 7).

The above fact is supported by various experimental studies: (a) experimental heating of CM chondrites has led to a high $\delta^{18}\text{O}$ composition due to mass-independent fractionation (Clayton & Mayeda 1999; Ivanova et al. 2010); (b) measurements of the oxygen isotopic composition of water from the Tagish Lake chondrite using stepped pyrolysis show a rise in $\delta^{18}\text{O}$ values up to $\sim 20\%$ at $\sim 1100 \text{ K}$ (Baker et al. 2002); (c) comparisons with Murchison and Orgueil point toward the smaller rise in $\delta^{18}\text{O}$ value to $\sim 8\%$ – 10% (Baker et al. 2002). Also the bulk whole rock of Orgueil and Tagish Lake has $\delta^{18}\text{O}$ values of $\sim 16\%$ – 19% , closer to the atmospheric value (Thiemens et al. 1995; Baker et al. 2002; Pack et al. 2017); and (d) the hydration–dehydration experiments by heating samples of Murchison and Mighei CM2 chondrites indicate that the oxygen isotopic composition of the precursor tends to be altered, becoming close to that of the hydration products (Ivanova et al. 2013). This shows that heating particles from hydrated carbonaceous chondrite parent bodies has the potential to lose ^{16}O during phyllosilicate dehydration and to enrich $\delta^{18}\text{O}$ by $\sim 5\%$ – 10% above the precursor value, bringing it close to 20% as seen in many cosmic spherules (Clayton & Mayeda 1999; Baker et al. 2002; Ivanova et al. 2010, 2013; Rudraswami et al. 2020; Suttle et al. 2020). These studies demonstrate that the unmelted MMs are susceptible to alteration, and as a consequence many particles have values similar

Table 2

Elemental Oxygen Mass Ablated (%) and the Total Ablated Mass of the Particle (%) (in Brackets) for Various Carbonaceous and Ordinary Chondritic Chemical Compositions, and for Various Sizes, ZAs, and Entry Velocities

Chondrite	Entry Velocity	Size (μm)	ZA = 0°	10°	20°	30°	40°	50°	60°	70°	80°
CI	11 km s ⁻¹	100	1[1]	1[1]	1[1]	1[1]	0[0]	0[0]	0[0]	0[0]	0[0]
		200	6[8]	5[8]	5[7]	3[5]	2[3]	1[2]	1[1]	1[1]	0[0]
		300	23[29]	22[28]	20[25]	16[20]	11[14]	6[8]	3[4]	1[2]	0[0]
		400	43[49]	42[48]	39[45]	34[40]	26[32]	17[22]	8[11]	2[4]	1[1]
		500	66[71]	65[70]	62[68]	58[64]	51[57]	40[47]	25[31]	10[13]	2[3]
		600	73[77]	72[76]	70[74]	66[71]	60[65]	50[56]	35[41]	16[20]	3[4]
		700	78[81]	77[80]	75[79]	71[76]	66[70]	56[62]	42[48]	21[27]	4[6]
	16 km s ⁻¹	100	29[36]	28[34]	24[31]	19[24]	12[17]	6[9]	2[4]	1[1]	0[0]
		200	84[86]	84[86]	81[84]	77[80]	69[73]	55[62]	36[43]	12[16]	1[2]
		300	95[95]	95[95]	94[95]	93[94]	90[91]	84[86]	69[74]	41[49]	6[9]
		400	96[96]	96[96]	96[96]	95[96]	95[95]	93[94]	86[88]	65[70]	19[25]
		500	97[97]	97[97]	97[97]	97[97]	96[97]	96[96]	95[95]	87[89]	48[55]
		600	97[98]	97[98]	97[97]	97[97]	97[97]	96[97]	95[96]	91[92]	60[66]
		700	97[98]	97[98]	97[98]	97[97]	97[97]	97[97]	96[96]	94[94]	67[72]
CM	11 km s ⁻¹	100	1[1]	1[1]	1[1]	1[1]	0[1]	0[0]	0[0]	0[0]	0[0]
		200	6[8]	5[7]	4[6]	3[5]	2[3]	1[2]	1[1]	0[1]	0[0]
		300	23[28]	22[27]	20[24]	15[20]	11[14]	6[8]	2[3]	1[1]	0[0]
		400	42[49]	42[48]	39[45]	33[39]	26[31]	17[21]	8[10]	2[3]	1[1]
		500	66[70]	65[69]	62[67]	58[63]	51[56]	40[46]	25[31]	9[13]	1[2]
		600	73[77]	72[76]	70[74]	66[71]	60[65]	50[56]	35[41]	15[20]	2[4]
		700	78[80]	77[80]	75[78]	72[75]	66[70]	56[62]	42[48]	21[26]	4[5]
	16 km s ⁻¹	100	28[35]	27[34]	24[30]	18[24]	12[16]	6[8]	2[3]	1[1]	0[0]
		200	84[86]	84[86]	81[84]	77[80]	69[73]	55[62]	36[43]	12[16]	1[2]
		300	94[94]	94[94]	94[94]	93[93]	90[91]	84[86]	69[73]	41[48]	6[8]
		400	96[96]	96[96]	95[96]	95[95]	94[95]	93[93]	86[88]	65[70]	19[24]
		500	97[98]	97[97]	97[97]	96[97]	96[96]	95[96]	94[94]	87[88]	48[55]
		600	98[98]	98[98]	98[98]	97[98]	97[97]	96[96]	95[95]	91[92]	59[65]
		700	98[99]	98[98]	98[98]	98[98]	97[97]	96[97]	95[96]	93[94]	67[72]
CV	11 km s ⁻¹	100	1[2]	1[2]	1[1]	1[1]	1[1]	0[1]	0[0]	0[0]	0[0]
		200	11[15]	11[14]	9[12]	7[9]	4[6]	2[3]	1[1]	0[1]	0[0]
		300	39[45]	38[44]	35[41]	30[36]	23[28]	14[18]	6[9]	2[3]	0[1]
		400	58[63]	57[62]	54[60]	49[55]	42[48]	31[37]	18[22]	6[8]	1[1]
		500	74[77]	73[76]	71[74]	67[71]	60[65]	50[56]	35[41]	16[20]	2[4]
		600	80[82]	79[82]	78[80]	74[77]	69[72]	59[64]	45[51]	24[29]	4[6]
		700	86[87]	86[87]	84[86]	82[84]	77[80]	70[73]	57[62]	36[42]	9[12]
	16 km s ⁻¹	100	60[66]	59[64]	55[61]	49[55]	39[46]	25[31]	11[15]	2[3]	0[1]
		200	91[91]	90[91]	89[90]	86[88]	81[83]	70[74]	51[57]	23[29]	2[3]
		300	95[95]	95[95]	94[95]	94[94]	93[93]	92[92]	85[86]	62[67]	16[21]
		400	96[97]	96[96]	96[96]	95[96]	95[95]	94[94]	92[93]	81[83]	37[44]
		500	98[98]	98[98]	97[98]	97[97]	96[97]	95[96]	94[94]	91[92]	61[66]
		600	98[99]	98[99]	98[98]	98[98]	97[97]	96[96]	95[95]	93[93]	72[75]
		700	99[99]	99[99]	99[99]	99[99]	98[98]	97[97]	96[96]	94[94]	83[85]
H	11 km s ⁻¹	100	2[4]	2[3]	2[3]	2[2]	1[2]	1[1]	1[1]	0[0]	0[0]
		200	25[41]	34[40]	31[36]	26[31]	19[23]	11[15]	5[7]	1[2]	1[1]
		300	56[62]	55[61]	52[58]	48[53]	40[46]	29[34]	16[20]	5[7]	1[1]
		400	70[74]	69[73]	67[71]	63[67]	56[61]	46[52]	31[36]	12[16]	2[3]
		500	81[83]	80[83]	78[81]	75[79]	70[74]	61[66]	47[53]	26[31]	5[7]
		600	88[90]	88[89]	87[88]	85[86]	81[83]	74[78]	63[68]	43[49]	13[17]
		700	91[92]	91[92]	90[91]	88[90]	86[87]	80[83]	71[75]	53[59]	21[25]
	16 km s ⁻¹	100	72[76]	71[75]	68[73]	62[68]	53[59]	39[46]	20[26]	5[7]	1[1]
		200	96[96]	96[96]	96[96]	95[96]	94[95]	90[91]	80[83]	56[62]	12[16]
		300	97[97]	97[97]	97[97]	97[97]	96[96]	95[96]	92[93]	79[82]	34[41]
		400	98[98]	98[98]	98[98]	97[98]	97[97]	96[97]	95[96]	90[91]	54[61]
		500	99[99]	99[99]	99[99]	98[98]	98[98]	97[97]	96[97]	95[95]	73[77]
		600	99[99]	99[99]	99[99]	99[99]	99[99]	98[98]	97[98]	96[96]	86[88]
		700	100[100]	100[100]	99[100]	99[99]	99[99]	99[99]	98[98]	97[97]	91[92]

Table 2
(Continued)

Chondrite	Entry Velocity	Size (μm)	ZA = 0°	10°	20°	30°	40°	50°	60°	70°	80°
L	11 km s ⁻¹	100	2[3]	2[3]	2[3]	1[2]	1[2]	1[1]	1[1]	0[0]	0[0]
		200	34[38]	33[37]	30[34]	25[29]	18[22]	10[13]	4[6]	1[2]	1[1]
		300	55[59]	54[59]	51[56]	46[51]	39[43]	28[32]	15[18]	4[6]	1[1]
		400	69[72]	69[72]	66[70]	62[66]	55[59]	45[49]	29[34]	12[15]	2[3]
		500	81[82]	80[82]	78[80]	75[77]	69[72]	60[64]	46[51]	25[29]	5[6]
		600	88[89]	88[89]	87[88]	84[86]	81[82]	74[76]	62[66]	42[47]	12[15]
		700	91[92]	91[91]	90[91]	88[89]	85[87]	80[82]	70[73]	52[56]	19[23]
	16 km s ⁻¹	100	72[75]	71[74]	67[71]	61[65]	51[56]	37[43]	19[23]	4[6]	1[1]
		200	96[96]	96[96]	95[96]	95[95]	94[94]	90[91]	80[82]	55[59]	11[14]
		300	97[97]	97[97]	97[97]	96[97]	96[96]	95[95]	92[93]	78[80]	33[38]
		400	98[98]	98[98]	98[98]	97[97]	97[97]	96[96]	95[95]	89[90]	53[58]
		500	99[99]	99[99]	98[99]	98[98]	98[98]	97[97]	96[96]	95[95]	72[75]
		600	99[99]	99[99]	99[99]	99[99]	99[99]	98[98]	97[97]	96[96]	86[87]
		700	100[100]	99[100]	99[100]	99[99]	99[99]	99[99]	98[98]	96[97]	91[92]
LL	11 km s ⁻¹	100	2[3]	2[3]	2[2]	1[2]	1[2]	1[1]	1[1]	0[0]	0[0]
		200	31[35]	30[34]	28[31]	23[26]	16[19]	9[12]	4[5]	1[2]	1[1]
		300	53[57]	52[56]	49[53]	44[48]	36[40]	26[29]	13[16]	4[5]	1[1]
		400	68[70]	67[70]	65[67]	60[63]	53[57]	42[46]	27[31]	10[13]	2[2]
		500	80[81]	79[80]	77[79]	74[76]	68[70]	59[62]	44[48]	23[26]	4[5]
		600	88[88]	87[88]	86[87]	84[85]	80[81]	73[75]	60[63]	39[44]	13[10]
		700	91[91]	90[91]	90[90]	88[88]	85[86]	79[81]	69[71]	49[53]	17[21]
	16 km s ⁻¹	100	70[72]	69[71]	65[68]	59[62]	49[53]	34[39]	17[20]	4[5]	1[1]
		200	96[96]	96[96]	95[95]	95[95]	94[94]	89[90]	78[80]	52[56]	10[12]
		300	97[97]	97[97]	97[97]	96[96]	96[96]	95[95]	92[92]	76[78]	30[34]
		400	98[98]	98[98]	97[98]	97[97]	97[97]	96[96]	95[95]	88[89]	50[55]
		500	99[99]	99[99]	98[99]	98[98]	98[98]	97[97]	96[96]	94[94]	70[73]
		600	99[99]	99[99]	99[99]	99[99]	99[99]	98[98]	97[97]	96[96]	85[86]
		700	99[100]	99[100]	99[99]	99[99]	99[99]	98[99]	98[98]	96[96]	90[91]

Note. Elemental oxygen ablation % [total ablation % of the particle].

to those seen in melted cosmic spherules, although the amount of water on the parent body will potentially control the final alteration value (Ivanova et al. 2010; Schrader & Davidson 2017; Suttle et al. 2020).

This may indicate that if Orgueil or Tagish Lake type chondrites dominate the MM flux then the chances of alteration due to atmospheric exchange may be of least significance. The scoriaceous, porphyritic, and barred particles have $\delta^{18}\text{O}$ values of $\sim 12\text{‰}$ – 25‰ , and so may have not undergone exchange. The average $\delta^{18}\text{O}$ has been seen to increase from scoriaceous to CAT spherules depending upon the peak temperature the particles have experienced, although the difference in average $\delta^{18}\text{O}$ value of porphyritic, barred, cryptocrystalline, and glass particles is small and governed by mass fractionation, indicating that similar precursor types are dominated by CC followed by OC sources (Rudraswami et al. 2020). However, the higher $\delta^{18}\text{O}$ of spherules with different textures, which exhibit an increase in $\delta^{18}\text{O}$ with peak temperature, is dominated by mass-dependent fractionation due to heating followed by stratospheric oxygen exchange (Rudraswami et al. 2020). In addition, the contribution of atmospheric exchange, if any, to the high $\delta^{18}\text{O}$ does not seem to have been established for the scoriaceous, porphyritic, barred, and cryptocrystalline spherules (Herzog et al. 1999; Engrand et al. 2005; Yada et al. 2005; Rudraswami et al. 2016c, 2020).

There is evidence of heterogeneous oxygen isotopic composition in the different constituents of chondritic components (Clayton et al. 1977; Jones et al. 2004; Ushikubo et al. 2012;

Marrocchi et al. 2018). The evolution of the oxygen isotopic composition of the dust particles in the solar nebula is echoed in the different components of the chondrites based on their interaction with the nebular gas reservoir (depleted in ^{16}O compared to dust), which was poorly constrained before becoming incorporated into planetesimals (Krot et al. 2005; Sakamoto et al. 2007; Kita et al. 2010). In brief, the amount of interaction of ^{16}O -rich or -poor particles with ^{16}O -depleted nebular gas followed by thermal processing will control the final composition of the particles that can shift to the terrestrial fractionation line (Kita et al. 2010). The proportion of solid/gas enrichment in the chondrite-forming region changes $\delta^{18}\text{O}$ in the following way, predicted by the CM84 model: 0% enrichment changes $\delta^{18}\text{O}$ by $\sim 15\text{‰}$, 50% by $\sim 21\text{‰}$, 100% by $\sim 25\text{‰}$, 150% by $\sim 29\text{‰}$, and 200% by $\sim 33\text{‰}$ (Wiens et al. 1999). In addition, the oxygen isotope composition of primordial water may have undergone aqueous alteration in carbonaceous chondrites, leading to high $\delta^{18}\text{O}$ values (Yurimoto et al. 2008). It is also likely that the oxygen isotope compositions of meteorites reaching the Earth's surface are limited, and have not seen the full extent of exchange between solid and gas/liquid as seen in MMs.

6. Implications

Based on $\delta^{18}\text{O}$ values, observations of oxygen isotopes from different type of MMs cannot be related straightforwardly to conventional chondritic groups. Care should also be exercised

in concluding that particles are not “primitive” materials and have been largely reprocessed during entry either by atmospheric exchange or by mass ablation. CABMOD indicates that there is a very low percentage of oxygen ablation in particles during entry until the peak temperature exceeds 2000 K (scoriaceous, porphyritic, barred, and cryptocrystalline particles have experienced <2000 K). At these temperatures the major elements Fe, Mg, and Si ablate (Vondrak et al. 2008; Rudraswami et al. 2015), releasing the associated oxygen and creating mass fractionation. In addition, the precursor properties are reflected in the increase of the $\delta^{18}\text{O}$ isotope value (Engrand et al. 1999, 2005). The glass and CAT spherules undergo significant O ablation, which plays a vital role in their high $\delta^{18}\text{O}$ values (Rudraswami et al. 2022). The different O-isotope compositions in MMs demonstrate the combination of diversity of precursor, dissimilar exchange during entry, and different degrees of O ablation. The diversity of the oxygen isotope composition of MMs is vital to the overall understanding of the solar system material, which otherwise would be incomplete. In addition, MMs are an important tool to probe the upper atmospheric oxygen fugacity and thus its fidelity in this approach depends upon the behavior of oxygen ablation and exchange during atmospheric entry. Also, comparison with samples received by sample return missions will shed light on the role of atmospheric reprocessing of the dust complex.

7. Conclusions

We present measurements of elemental oxygen ablation and the oxygen isotope ratios of MMs, combined with the Chemical Ablation Model (CABMOD), to decipher the contribution of the atmospheric mixing and evaporative mass loss during entry. The results show that oxygen elemental ablation is minimal (<5%) if the particle temperature does not reach 2000 K, so that scoriaceous, porphyritic, barred, and cryptocrystalline particles should have oxygen isotope compositions close to their parent precursors. The large $\delta^{18}\text{O}$ values of MMs from partially heated scoriaceous to glass (except CAT) spherules suggest that their precursors are distinctive primitive carbonaceous chondrites that were either altered by nebular gas during formation and/or aqueously altered in their parent bodies. The observed large $\delta^{18}\text{O}$ values in many unmelted MMs do not seem to have experienced alteration during atmospheric entry, either by exchange or by mass ablation, but they may have been contributed by their precursors based on oxygen isotope data on MMs. These observations seem to corroborate the paradigm that hydrated carbonaceous chondrites have large $\delta^{18}\text{O}$ values, thereby revealing the dominant contribution of water-rich C-type asteroids to the flux of MMs.

This work is funded by ISRO-Respond project GAP3332 (ISRO-Respond) and GAP2175 (MOES-PMN). J.D.C.S., W.F., and J.M.P.C. were supported by the European Research Council (project 291332-CODITA). This is NIO’s contribution number: 6973.

Appendix Supplementary Material

Compiled oxygen isotope data (423) from the literature for various types of MMs (404) analyzed using multiple techniques including Isotope Ratio Mass Spectrometry (IRMS) and in situ ion microprobe analyses (Clayton et al. 1986;

Engrand et al. 1999, 2005; Taylor et al. 2005; Yada et al. 2005; Matrajt et al. 2006; Suavet et al. 2010; Cordier et al. 2011, 2012; Rudraswami et al. 2015, 2020; Van Ginneken et al. 2017; Goderis et al. 2020; Fischer et al. 2021).

ORCID iDs

N. G. Rudraswami  <https://orcid.org/0000-0002-3375-9860>

W. Feng  <https://orcid.org/0000-0002-9907-9120>

J. M. C. Plane  <https://orcid.org/0000-0003-3648-6893>

References

- Baker, L., Franchi, I. A., Wright, I. P., & Pillinger, C. T. 2002, *M&PS*, **37**, 977
- Bones, D. L., Carrillo Sánchez, J. D., Connell, S. D. A., et al. 2022, *E&SS*, **9**, e2021EA001884
- Bones, D. L., Carrillo-Sánchez, J. D., Kulak, A. N., & Plane, J. M. C. 2019, *P&SS*, **179**, 104725
- Bones, D. L., Gómez Martín, J. C., Carrillo Sánchez, J. D., Dobson, A. J., & Plane, J. M. C. 2018, *GRL*, **45**, 7765
- Bones, D. L., Gómez Martín, J. C., Empson, C. J., et al. 2016, *RSci*, **87**, 12
- Brownlee, D. E., Bates, B., & Schramm, L. 1997, *M&PS*, **32**, 157
- Carrillo-Sánchez, J. D., Bones, D. L., Douglas, K. M., et al. 2020, *P&SS*, **187**, 104926
- Carrillo-Sánchez, J. D., Plane, J. M. C., Feng, W., Nesvorný, D., & Janches, D. 2015, *GRL*, **42**, 6518
- Clayton, R. N., & Mayeda, T. K. 1999, *GeCoA*, **63**, 2089
- Clayton, R. N., Mayeda, T. K., & Brownlee, D. E. 1986, *E&PSL*, **79**, 235
- Clayton, R. N., Onuma, N., Grossman, L., & Mayeda, T. K. 1977, *E&PSL*, **34**, 209
- Cordier, C., & Folco, L. 2014, *GeCoA*, **146**, 18
- Cordier, C., Folco, L., Suavet, C., Sonzogni, C., & Rochette, P. 2011, *GeCoA*, **75**, 5203
- Cordier, C., Suavet, C., Folco, L., Rochette, P., & Sonzogni, C. 2012, *GeCoA*, **77**, 515
- Defouilloy, C., Nakashima, D., Joswiak, D., et al. 2017, *E&PSL*, **465**, 145
- Engrand, C., McKeegan, K. D., & Leshin, L. A. 1999, *GeCoA*, **63**, 2623
- Engrand, C., McKeegan, K. D., Leshin, L. A., & Herzog, G. F. 2005, *GeCoA*, **69**, 5365
- Fischer, M. B., Oeser, M., Weyer, S., et al. 2021, *PaPa*, **36**, e2020PA004159
- Flynn, G. J. 1989a, *LPSC*, **19**, 673
- Flynn, G. J. 1989b, *Icar*, **77**, 287
- Flynn, G. J., Consolmagno, G. J., Brown, P., & Macke, R. J. 2018, *Chem. Erde*, **78**, 269
- Flynn, G. J., & Sutton, S. R. 1990, *LPSC*, **20**, 335
- Genge, M., Larsen, J., van Ginneken, M., & Suttle, M. 2016, *Geol*, **45**, 119
- Genge, M. J. 2017a, *M&PS*, **52**, 1000
- Genge, M. J. 2017b, *GRL*, **44**, 1679
- Genge, M. J., Davies, B., Suttle, M. D., van Ginneken, M., & Tomkins, A. G. 2017, *GeCoA*, **218**, 167
- Genge, M. J., Engrand, C., Gounelle, M., & Taylor, S. 2008, *M&PS*, **43**, 497
- Genge, M. J., Gileski, A., & Grady, M. M. 2005, *M&PS*, **40**, 225
- Genge, M. J., Grady, M. M., & Hutchison, R. 1997, *GeCoA*, **1997**, 5149
- Goderis, S., Soens, B., Huber, M. S., et al. 2020, *GeCoA*, **270**, 112
- Gómez Martín, J. C., Bones, D. L., Carrillo-Sánchez, J. D., et al. 2017, *ApJ*, **836**, 212
- Goodrich, C. A., Zolensky, M. E., Fioretti, A. M., et al. 2019, *M&PS*, **54**, 2769
- Gounelle, M., Chaussidon, M., Morbidelli, A., et al. 2009, *PNAS*, **106**, 6904
- Gounelle, M., Engrand, C., & Maudret, M. 2005, *M&PS*, **40**, 917
- Greshake, A., Bischoff, A., & Hoppe, P. 1996, *M&PS*, **31**, 739
- Hashimoto, A. 1983, *Geochim*, **17**, 111
- Herzog, G. F., Xue, S., Hall, G. S., et al. 1999, *GeCoA*, **63**, 1443
- Ikeda, Y., & Prinz, M. 1993, *GeCoA*, **57**, 439
- Ireland, T. R., Avila, J., Greenwood, R. C., Hicks, L. J., & Bridges, J. C. 2020, *SSRv*, **216**, 1
- Ivanova, M. A., Lorenz, C. A., Franchi, I. A., Bychkov, A. Y., & Post, J. E. 2013, *M&PS*, **48**, 2059
- Ivanova, M. A., Lorenz, C. A., Nazarov, M. A., et al. 2010, *M&PS*, **45**, 1108
- Jones, R. H., Leshin, L. A., Guan, Y., et al. 2004, *GeCoA*, **68**, 3423
- Kebukawa, Y., Ito, M., Zolensky, M. E., et al. 2019, *NatSR*, **9**, 3169
- King, A. J., Bates, H. C., Krietsch, D., et al. 2019, *Geochem*, **79**, 125531
- Kita, N. T., Nagahara, H., Tachibana, S., et al. 2010, *GeCoA*, **74**, 6610
- Krot, A. N., Hutcheon, I. D., Yurimoto, H., et al. 2005, *APJ*, **622**, 1333
- Love, S. G., & Brownlee, D. E. 1991, *Icar*, **89**, 26

- Love, S. G., & Brownlee, D. E. 1993, *Sci*, **262**, 550
- Love, S. G., Joswiak, D. J., & Brownlee, D. E. 1994, *Icar*, **111**, 227
- Marrocchi, Y., Villeneuve, J., Batanova, V., Piani, L., & Jacquet, E. 2018, *E&PSL*, **496**, 132
- Matrajt, G., Guan, Y., Leshin, L., et al. 2006, *GeCoA*, **70**, 4007
- Maurette, M., Jehanno, C., Robin, E., & Hammer, C. 1987, *Natur*, **328**, 699
- Maurette, M., Olinger, C., Christophe, M., et al. 1991, *Natur*, **351**, 44
- Messenger, S., Keiko Nakamura, M., Keller, L. P., & Clemett, J. S. 2015, *M&PS*, **50**, 1468
- Nesvorný, D., Janches, D., Vokrouhlický, D., et al. 2011, *ApJ*, **743**, 129
- Noguchi, T., Ohashi, N., Tsujimoto, S., et al. 2015, *E&PSL*, **410**, 1
- Onoue, T., Nakamura, T., Haranosono, T., & Yasuda, C. 2011, *Geol*, **39**, 567
- Pack, A., Höweling, A., Hezel, D., et al. 2017, *NatCo*, **8**, 15702
- Plane, J. M. C. 2012, *ChSRv*, **41**, 6507
- Plane, J. M. C., Feng, W. H., & Dawkins, E. C. M. 2015, *ChRv*, **115**, 4497
- Prasad, M. S., Rudraswami, N. G., De Araujo, A., Babu, E. V. S. S. K., & Vijaya Kumar, T. 2015, *M&PS*, **50**, 1013
- Prasad, M. S., Rudraswami, N. G., & Panda, D. K. 2013, *JGR*, **118**, 2381
- Reshma, K., Prasad, M. S., & Rudraswami, N. 2013, *JESS*, **122**, 1161
- Rochette, P., Folco, L., Suavet, C., et al. 2008, *PNAS*, **105**, 18206
- Rojas, J., Duprat, J., Engrand, C., et al. 2021, *E&PSL*, **560**, 116794
- Rowe, M. W., Clayton, R. N., & Mayeda, T. K. 1994, *GeCoA*, **58**, 5341
- Rudraswami, N. G., Fernandes, D., Naik, A. K., et al. 2018, *ApJ*, **853**, 38
- Rudraswami, N. G., Genge, M. J., Marrocchi, Y., Villeneuve, J., & Taylor, S. 2020, *JGRP*, **125**, e2020JE006414
- Rudraswami, N. G., Marrocchi, Y., Prasad, M. S., et al. 2019, *M&PS*, **54**, 1347
- Rudraswami, N. G., Prasad, M. S., Dey, S., et al. 2015, *ApJ*, **814**, 78
- Rudraswami, N. G., Shyam Prasad, M., Dey, S., et al. 2016a, *ApJ*, **831**, 197
- Rudraswami, N. G., Shyam Prasad, M., Dey, S., et al. 2016b, *ApJS*, **227**, 15
- Rudraswami, N. G., Shyam Prasad, M., Jones, R. H., & Nagashima, K. 2016c, *GeCoA*, **194**, 1
- Rudraswami, N. G., Suttle, M. D., Marrocchi, Y., Taylor, S., & Villeneuve, J. 2022, *GeCoA*, **325**, 1
- Sakamoto, N., Seto, Y., Itoh, S., et al. 2007, *Sci*, **317**, 231
- Schrader, D. L., & Davidson, J. 2017, *GeCoA*, **214**, 157
- Steven, G., Bastien, S., Matthew, S. H., et al. 2020, *GeCoA*, **270**, 112
- Suavet, C., Alexandre, A., Franchi, I. A., et al. 2010, *E&PSL*, **293**, 313
- Suttle, M. D., Dionnet, Z., Franchi, I., et al. 2020, *E&PSL*, **546**, 116444
- Suttle, M. D., Folco, L., Genge, M. J., et al. 2019, *GeCoA*, **245**, 352
- Taylor, S., Alexander, C.M.O.'D., Delaney, J., et al. 2005, *GeCoA*, **69**, 2647
- Taylor, S., & Brownlee, D. E. 1991, *Metic*, **26**, 203
- Taylor, S., Delaney, J., & Herzog, G. 2010, *LPSC*, **41**, 1205
- Taylor, S., Lever, J. H., & Harvey, R. P. 1998, *Natur*, **392**, 899
- Taylor, S., Lever, J. H., & Harvey, R. P. 2000, *M&PS*, **35**, 651
- Tenner, T., Nakashima, D., Ushikubo, T., Kita, N., & Weisberg, M. 2015, *GeCoA*, **148**, 228
- Thiemens, M. H., Jackson, T., Zipf, E. C., Erdman, P. W., & Van Egmond, C. 1995, *Sci*, **270**, 969
- Tomkins, A., Bowlt, L., Genge, M., et al. 2016, *Natur*, **533**, 235
- Tonui, E., Zolensky, M., Hiroi, T., et al. 2014, *GeCoA*, **126**, 284
- Toppani, A., & Libourel, G. 2003, *GeCoA*, **67**, 4621
- Toppani, A., Libourel, G., Engrand, C., & Maurette, M. 2001, *M&PS*, **36**, 1377
- Ushikubo, T., & Kimura, M. 2021, *GeCoA*, **293**, 328
- Ushikubo, T., Kimura, M., Kita, N. T., & Valley, J. W. 2012, *GeCoA*, **90**, 242
- Van Ginneken, M., Gattacceca, J., Rochette, P., et al. 2017, *GeCoA*, **212**, 196
- Vondrak, T., Plane, J. M. C., Broadley, S., & Janches, D. 2008, *ACP*, **8**, 7015
- Wiens, R. C., Huss, G. R., & Burnett, D. S. 1999, *M&PS*, **34**, 99
- Yada, T., Nakamura, T., Noguchi, T., et al. 2005, *GeCoA*, **69**, 5789020JE006414
- Yada, T., Nakamura, T., Takaoka, N., et al. 2004, *EP&S*, **56**, 67
- Yurimoto, H., Krot, A. N., Choi, B. G., et al. 2008, *RvMG*, **68**, 141